metals

MDPI

Article

Alternative Approach for the Intercritical Annealing of (Cr, Mo, V)-Alloyed TRIP-Assisted Steel before Austempering

Vadym Zurnadzhy [1], Vasily Efremenko [1,2,*], Ivan Petryshynets [2], Manuele Dabalà [3], Mattia Franceschi [3], Kaiming Wu [4], František Kováč [2], Yuliia Chabak [1,2], Viktor Puchy [2] and Michail Brykov [5]

1 Physics Department, Pryazovskyi State Technical University, 87555 Mariupol, Ukraine
2 Institute of Materials Research, Slovak Academy of Sciences, 04001 Kosice, Slovakia
3 Department of Industrial Engineering, University of Padova, 35131 Padova, Italy
4 The State Key Laboratory of Refractories and Metallurgy, Hubei Province Key Laboratory of Systems Science in Metallurgical Process, International Research Institute for Steel Technology, Collaborative Innovation Center for Advanced Steels, Wuhan University of Science and Technology, Wuhan 430081, China
5 Welding Department, National University "Zaporizhzhia Polytechnic", 69063 Zaporizhzhia, Ukraine
* Correspondence: efremenko_v_g@pstu.edu or vgefremenko@gmail.com

Abstract: TRIP-assisted C-Si-Mn steels are usually subjected to austempering with a preliminary intercritical annealing that is targeted at the multi-phase structure with 40–60 vol.% of proeutectoid ferrite. The kinetics and the mechanism of phase-structural transformations can be impacted due to the additional alloying of TRIP-assisted steel by the strong carbide forming elements, thus necessitating an alternative approach for the selection of intercritical annealing parameters. This issue is analyzed in the present work, which investigates the effect of the temperature of intercritical annealing on the "Structure/Properties" correlations in 0.2 wt.% C-Si-Mn-Nb steel additionally alloyed by 0.55 wt.% Cr, 0.20% Mo, and 0.11 wt.% V. The annealing temperature ranged from 770 °C to 950 °C, and austempering was performed at 350 °C for 20 min. It was observed that the addition of the (Cr, Mo, and V) complex significantly improved the steel hardenability. However, the annealing of steel at 770 °C (to gain 50 vol.% of proeutectoid ferrite) resulted in the precipitation of coarse cementite lamellas during bainite transformation, thus lowering the amount of retained austenite (RA) and decreasing the strength and ductility of the steel. At higher annealing temperatures, carbide-free bainite was formed, which presented a 2.5–3.5 times increase in the RA volume fraction and a 1.5 times increase in the RA carbon content. The optimal combination of the mechanical properties (UTS of 1040 MPa, TEL of 23%, V-notch impact toughness of 95 J/cm^2, PSE of 23.9 GPa·%) referred to annealing at a temperature close to the Ac_3 point, resulting in a structure with 5 vol.% ferrite and 9 vol.% RA (the residue was carbide-free bainite). This structure presented an extended manifestation of the TRIP effect with an enhanced strain hardening rate due to strain-induced martensite transformation. The impact of the alloying elements on the carbon activity in austenite served as the basis for the analysis of structure formation.

Keywords: TRIP-assisted steel; ferrite; austenite; bainite; mechanical behavior; fracture

check for updates

Citation: Zurnadzhy, V.; Efremenko, V.; Petryshynets, I.; Dabalà, M.; Franceschi, M.; Wu, K.; Kováč, F.; Chabak, Y.; Puchy, V.; Brykov, M. Alternative Approach for the Intercritical Annealing of (Cr, Mo, V)-Alloyed TRIP-Assisted Steel before Austempering. *Metals* **2022**, *12*, 1814. https://doi.org/10.3390/met12111814

Academic Editor: Marcello Cabibbo

Received: 30 September 2022
Accepted: 12 October 2022
Published: 26 October 2022

Publisher's Note: MDPI stays neutral with regard to jurisdictional claims in published maps and institutional affiliations.

Copyright: © 2022 by the authors. Licensee MDPI, Basel, Switzerland. This article is an open access article distributed under the terms and conditions of the Creative Commons Attribution (CC BY) license (https://creativecommons.org/licenses/by/4.0/).

1. Introduction

Current approaches to the design of automobiles and other vehicles necessitate the use of lightweight materials with improved mechanical and technological properties. The use of such materials results in a reduction in the weight of vehicles, increased efficiency, and a reduction in greenhouse gas emissions. Currently, the industry is actively employing a wide variety of steels, which includes the advanced high-strength steels of the first generation [1,2]. Among them, the TRIP-assisted steels have attracted the attention of researchers owing to their improved mechanical behavior and cost-effective alloying [3]. The main characteristic of TRIP-assisted steels is their ability to transform into strain-induced martensite [4], which helps in enhancing both strength and formability [5]. The TRIP effect

is achieved in steels with low contents of carbon (0.1–0.2 wt.%) and alloying elements (Mn, Ni, and Cr) [1,6,7]. This behavior is facilitated by alloying steel with a higher amount of silicon and (or) aluminum and through a special heat treatment (austempering), during which austenite (A) is enriched with carbon thus stabilizing to phase transformations. Even in low-carbon low-alloy steel [8], the carbon content in austenite attains a high value (up to 1.0 wt.%), ensuring the retention of 5–15 vol.% austenite, which is atypical for such steels [9,10]. During deformation, retained austenite (RA) transforms into martensite and provides the TRIP effect, which is considered to be a complex mechanism of metal adaptation to external load [11–13], contributing to enhancement in mechanical behavior [14], formability [15,16], wear resistance [17,18], fatigue resistance [19,20], etc.

The fundamental concept of TRIP-assisted steel alloying entails the use of inexpensive elements such as Si, Mn, and Al [1,6,15]. The characteristics of TRIP-assisted steels are further enhanced by the micro-addition of V, Nb, Ti, and Mo through grain refinement and precipitation strengthening [21–24]. According to Oja et al. [21], the micro-addition of Nb and V to 0.2 wt.% C-Si-Al-Mo-Cu TRIP-assisted steel improved elongation and ductility via grain refinement. Additionally, it was concluded [21] that Nb is more effective than vanadium in respect of grain size control. Mohrbacher et al. [24] reported that due to the involvement of various strengthening mechanisms, 0.03 wt.% Nb increased the tensile strength of dual-phase DP980 HD steel by nearly 180 MPa. Moreover, precipitation hardening along with grain refinement facilitates a more uniform strain distribution in Nb-containing TRIP-assisted steel, which delays the necking in the specimen toward higher deformation [24]. Abbasi et al. [25] added 0.04 wt.% Nb and 0.08 wt.% Mo to V-containing TRIP-assisted steel and discovered that the (Nb, V, Mo)C precipitates have improved thermal stability with a low tendency for coarsening during heat treatment, thus enabling effective pinning of the mobile grain boundaries.

TRIP-assisted steel is rarely alloyed with other elements (Cr, Ni, Cu, and B), primarily to increase its hardenability [15,21,26–29]. It was reported [15] that alloying with 1 wt.% Cr improved the formability of the TRIP-assisted steel after isothermal holding at temperatures below the martensite-finish temperature. Kučerová et al. [26] noticed an increase in ductility of 0.2 wt.% C-0.6 wt.% Mn-2 wt.% Si-0.04 wt.% Nb after the addition of 0.8 wt.% Cr. However, in this case, due to the presence of pearlite and low amounts of bainite and RA, the microstructure was not typical for TRIP-steels. As a consequence of the lack of systematic data, a further study on the effect of the above elements on the transformation behavior and mechanical properties of TRIP-assisted steels is needed.

The multi-phase structure consisting of proeutectoid ferrite, bainite, and retained austenite is the target of the conventional heat treatment of TRIP-assisted steels. Heat treatment includes two stages: (1) intercritical annealing (IA) and (2) austempering (isothermal holding for austenite→bainite transformation). In the first stage, carbon diffuses from the α-phase to γ-phase, enriching the latter [30]. Furthermore, the alloying elements partition, enriching austenite with the gamma-stabilizer (Mn) and ferrite by alpha-stabilizers (Si, Al) [31,32]. According to finding in Reference [33], holding low-carbon TRIP-assisted steel at 770 °C resulted in austenite with a manganese content that is 2.6 times that of ferrite. Meanwhile, ferrite was 13% enriched in silicon, as compared to austenite. Therefore, intercritical annealing provides a substantial chemical stabilization of austenite, which is crucial for the kinetics of its subsequent transformation [30,34–36]. The enrichment of austenite with C and Mn depends on the austenite/ferrite volume ratio in the intercritical range, which in turn is influenced by the annealing temperature relative to the Ac_1 and Ac_3 points. The IA temperature is one of the key parameters of the heat treatment process since it predetermines (a) the chemical composition of austenite before austempering holding (stage 2) and (b) the volume fraction of proeutectoid ferrite in the resulting structure. According to the conventional approach [1,37,38], the IA temperature is chosen to acquire 40–65 vol.% of polygonal ferrite, providing the high ductility required for optimal steel formability. In support of this, Guzman and Monsalve [39] recently reported that 57 vol.% of ferrite is optimal for the mechanical behavior of CMnSiAl TRIP-assisted steel. However,

adding other alloying elements (Cr, Mo, V, etc.) into TRIP-assisted steel may alter the thermodynamic activity of carbon in the γFe and αFe phases, accelerating the formation of cementite during bainite transformation [40]. As this scenario may lower the RA amount and deteriorate steel ductility, it should be avoided by modifying the heat treatment strategy (including the target ferrite amount). Therefore, to optimize the austempering parameters, it is crucial to study the mechanism and kinetics of bainitic transformation in complex alloyed TRIP-assisted steels. In light of the aforementioned observations, the present work is dedicated to the evaluation of a (Cr, Mo, and V)-added TRIP-assisted steel exposed to an austempering treatment, with a specific focus on the impact of an intercritical annealing temperature on the "structure/mechanical properties" relationships.

2. Materials and Methods

2.1. Material and its Manufacturing Process

The experimental material was steel containing 0.20 wt.% C, 1.79 wt.% Si, 1.73 wt.% Mn, 0.55 wt.% Cr, 0.20 wt.% Mo, 0.11 wt.% V, 0.045 wt.% Nb, 0.009 wt.% S, 0.013 wt.% P, and Fe balance. Steel was smelted in the open air in a 120-kg high-frequency induction furnace using steel scrap, pig iron, and the master alloys (Fe-Mn, Fe-Si, Fe-Cr, Fe-Mo, Fe-V, Fe-Nb). The smelt was deoxidized by aluminum and poured into graphite molds with an inner diameter of 50 mm. The cast ingots were welded into the single rod and then electro-slag remelted to produce an 80 mm diameter cast billet. This billet was subjected to preliminary forging with a final hot rolling to produce a strip with a thickness of 15 mm. The strip was soft-annealed at 900 °C and slowly cooled inside the switched-off furnace before machining. As shown in Figure 1a, the annealed steel exhibited mostly a fine-grained "Ferrite (F) + Pearlite (P)" structure (ferrite grain size of 8.1 ± 0.6 μm) with minor bainite areas. The standard heat treatment (water quenching from 950 °C followed by tempering at 600 °C for 2 h (Q + T)) was also performed as a reference to reveal the advantage of austempering over the routing heat treatment in the mechanical properties. After (Q + T) treatment the steel had a structure of tempered lath martensite with the coarse globular carbide particles seen in the optical microscope (Figure 1b).

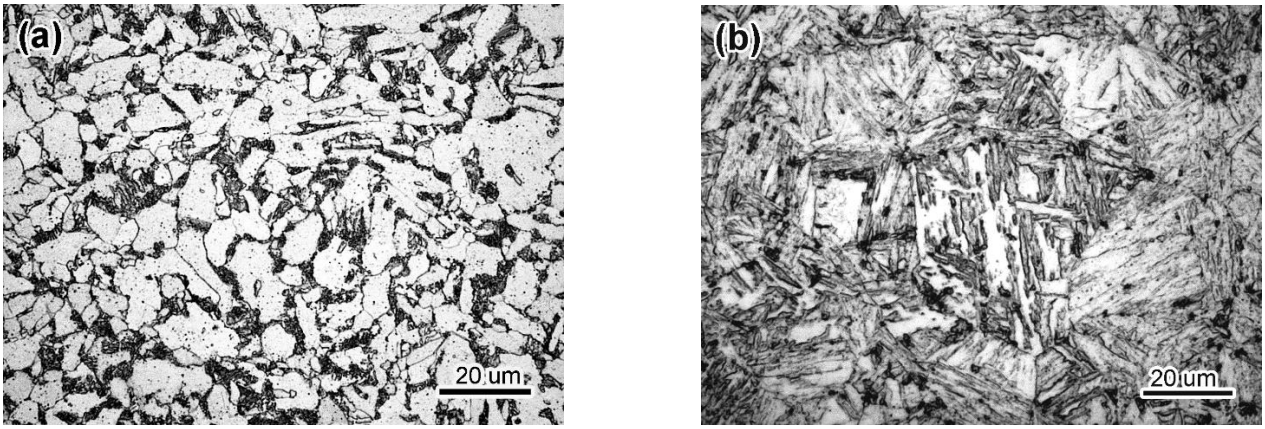

Figure 1. The microstructure of the experimental steel after (**a**) annealing and (**b**) standard heat treatment (quenching + tempering).

2.2. Heat Treatment Mode Selection

The specimens were subjected to austempering, which involved austenitizing of the specimens for 10 min in an electric furnace and further holding in a molten metal bath (60 wt.% Sn + 40 wt.% Pb) with a final air cooling. The selection of heat treatment modes included the determination of austenitizing temperatures (T_A) and the austempering process parameters. The variation in T_A aimed to obtain different (vol.%) austenite/ferrite ratios before the austempering holding. The positions of critical points Ac_1 (760 °C) and Ac_3 (930 °C) previously discovered for the steel under study [33] were used to select the appropriate

values of T_A. Accordingly, austenitization was performed at 770 °C, 830 °C, and 900 °C, corresponding to 50%F + 50%A (at 770 °C), 25%F + 75%A (at 830 °C), and 5%F + 95%A (at 900 °C) [33]. Furthermore, to ensure 100% austenite before the austempering holding, 950 °C was chosen as the austenitizing temperature.

The analysis of the kinetics of austenite phase transformation, emphasizing the lower bainite formation (which implies the holding temperature to be close to Ms) [41], led to the derivation of the austempering parameters (holding temperature and holding duration). A computer simulation was performed for this purpose using "JMatPro" (Version 7, Sente Software, Guildford, UK) software (presuming the grain size of 10 µm). Figure 2 presents the "Temperature-Time-Transformation" (TTT) diagrams for austenitization at 770 °C (blue lines) and 900 °C (pink lines), which are close to the lower and upper limits of the intercritical temperature range. As can be seen, the TTT-diagram performs the divorced areas of pearlite and bainite transformations. When T_A is 770 °C, the bainite and martensite transformations begin at Bs = 458 °C and Ms = 252 °C, respectively, and the incubation period at the "noses" of the pearlite area (612 °C) and bainite area (400 °C) was estimated to be 22 s and 12 s, respectively. At a T_A of 900 °C, bainite and martensite transformations start at higher temperatures (Bs = 511 °C, Ms = 349 °C) while austenite exhibits reduced stability with a minimum incubation period of 17 s at the pearlitic "nose" (618 °C) and 2 s at the bainitic "nose" (438 °C). For comparison, the plot in Figure 2 presents a black line which refers to the onset of austenite transformation in the previously examined similar C-Si-Mn-Nb TRIP-steel [42] that is not alloyed by Cr, Mo, and V. It is evident that (Cr, Mo, and V)-alloying significantly increases the stability of austenite, especially in the pearlitic transformation area. Based on the TTTs, the austempering temperature was selected as 350 °C for all experimental regimes to be either slightly higher than (at T_A = 770 °C) or equal (at T_A = 900 °C) to the Ms temperature. Accordingly, to ensure the bainite transformation's completion (99.9%) at different austenitization temperatures, a holding duration of 1200 s was selected.

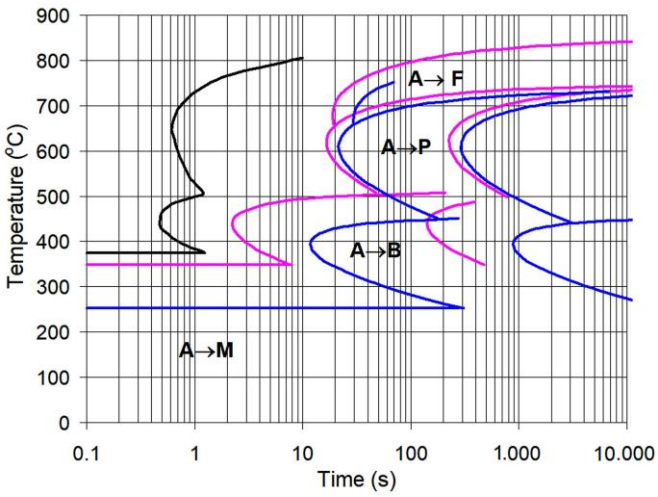

Figure 2. TTT diagrams for steel austenitized at 770 °C (blue lines) and 900 °C (pink lines). The lines correspond to the start (0.1 vol. %) and finish (99.9 vol.%) of the transformation. The black line refers to (Cr, Mo, and V)-free steel (T_A = 900 °C) (A, F, P, B, M are austenite, ferrite, pearlite, bainite, and martensite, respectively).

2.3. Structure-Properties Evaluation

The heat-treated specimens were mechanically tested at room temperature using a servo-driven tensile machine and a Charpy impact machine. The tensile specimens had a 5 mm diameter and 30 mm long gauge, the V-notched impact specimens were 55 mm long and of 7.5 mm × 10 mm in the cross-section. The loading rate at the tensile testing was 5 mm/min. For each heat treatment mode, three tensile and three impact specimens were used, and the average of the results was noted. The microstructure was observed on

the specimens mirror-polished according to the standard metallographic technique and etched by 4 vol.% Nital reagent. To characterize the microstructure, an optical microscope (OM), Carl Zeiss Axiovert 40 MAT (Zeiss AG, Jenna, Germany), and a scanning electron microscope (SEM) JEOL JSM-7000F (JEOL, Tokyo, Japan), equipped with an EDX-detector INCAx-sight (Oxford Instruments, Abingdon, UK), were used. The point EDS analysis of the precipitates was performed at ten points in different sights with further averaging the results. The fine structure of the heat-treated specimens was investigated using a transmission electron microscope (TEM) JEOL JEM 100C-XII (JEOL, Tokyo, Japan). To make the foils for TEM characterization, the TEM specimens were ground to 0.10–0.15 mm with consequent electro-polishing at minus 30 °C in a 6.3 vol.% perchloric acid solution. The phase identification was performed using X-ray diffraction applying a Siemens D500 (Siemens, Munich, Germany) diffractometer with a CuK_{α} radiation equipped with the monochromator on the detector side (tube parameters: 40 kV and 30 mA, step: 0.025°, dwell time: 3 s, scanning speed: 0.0083 °/s). The volume fraction of RA and the carbon content of RA were derived from the XRD patterns according to the procedure described in Reference [43].

3. Results

3.1. Mechanical Properties Assessment

Figure 3 shows the engineering strain–stress curves that depict the axial tensile behavior of the specimens. For each austenitizing temperature, the specimens featured continuous yielding with a neck formation. Notably, with the increase in T_A, the load decreasing on the non-uniform deformation interval became more pronounced, thus reflecting higher area reduction (AR) before the specimen fracture.

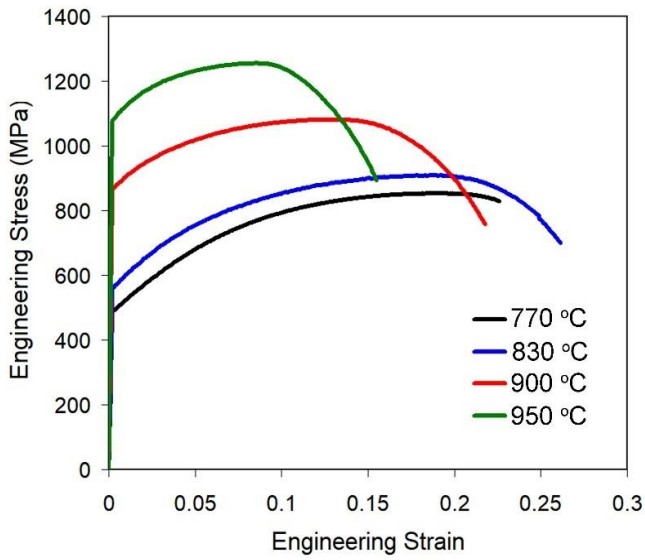

Figure 3. "Engineering strain–Engineering stress" curves depending on the temperature of the intercritical annealing.

Figure 4 presents the mechanical properties of steel. The dashed lines depict the level of the (Q + T) heat treatment. Figure 4a demonstrates a monotonic increase in the strength indicators of the austempered specimens as the austenitizing temperature increased from 770 °C to 950 °C. In particular, the yield tensile strength (YTS) increased from 482 MPa to 1074 MPa while the ultimate tensile strength (UTS) increased from 821 MPa to 1207 MPa. The ultimate tensile strength (1040 MPa) reached the level of (Q + T)-treated steel after austempering at T_A = 900 °C, while the yield strength (900 MPa) was lower by 65 MPa. YTS and UTS exceeded the (Q + T) level when the austenitizing temperature increased to 950 °C. The difference between UTS and YTS decreased with an increase in T_A. Accordingly,

the YTS/UTS ratio increased from 0.59 to 0.89, which is lower than that of the (Q + T) heat treatment.

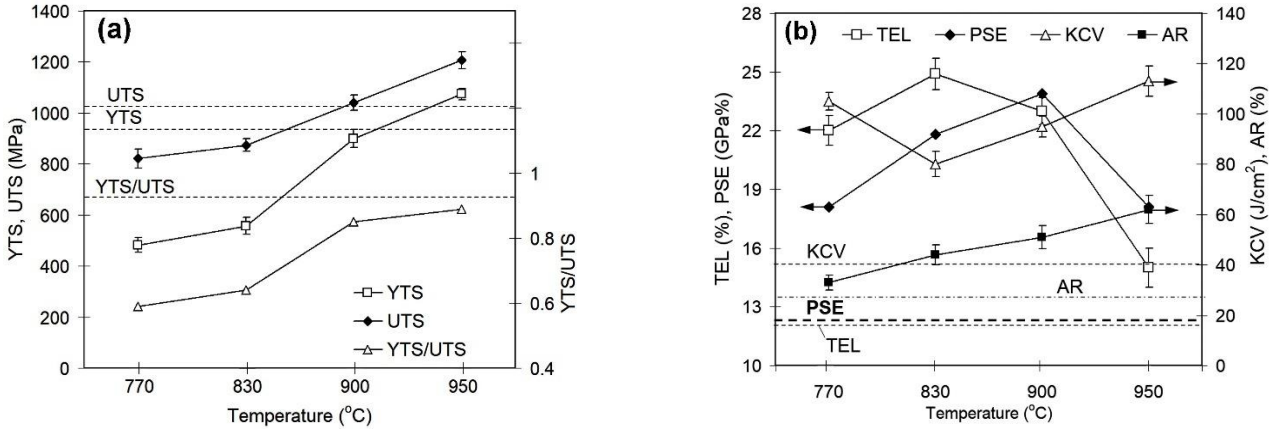

Figure 4. Effect of austenitizing temperature on the mechanical properties of the austempered specimens (**a**) YTS, UTS, YTS/UTS ratio and (**b**) TEL, PSE, KCV, AR.

The total elongation (TEL) values varied non-monotonically, with a maximum value (25%) referred to as T_A = 830 °C (Figure 4b). TEL decreased to 23% at T_A = 900 °C, which was higher than that at T_A = 770 °C (22%). It is noteworthy that the TEL values for T_A = 770–900 °C were nearly two times those of the (Q + T)-treatment (12%). The TEL was considerably reduced to 15% as a consequence of the increase in T_A to 950°C. The area reduction tended to increase gradually with increasing T_A, from 33% (at 770 °C) to 62% (at 950 °C). Impact toughness (KCV) varied transversally with TEL. The value of KCV, which was 105 J/cm^2 at T_A = 770 °C, dropped to 58 J/cm^2 at T_A = 830 °C and then rose to 113 J/cm^2 with a further increase in T_A. It must be emphasized that the austempered specimens performed 1.4–2.8 times higher impact toughness as compared to (Q + T)-treated specimens (KCV = 41 J/cm^2), regardless of the austenitizing temperature. Figure 4b displays the influence of T_A on the PSE index (Product of Strength and Elongation), which is used to characterize the combination of "strength/ductility". The PSE value rose from 18.1 GPa·% at T_A = 770 °C to 23.9 GPa·% at T_A = 900 °C, which subsequently decreased to 15.8 GPa·% at T_A = 950 °C. All these values remarkably exceeded the level of the (Q + T)-treatment (12.4 GPa·%).

3.2. Structure and Phase Characterization

Figure 5 illustrates the microstructures of the heat-treated specimens. Figure 5a depicts the structure produced by the austempering at T_A = 770 °C, which consists of polyhedral grains of proeutectoid ferrite (PF) and bainite areas. While bainite has a mostly lamellar pattern (LB), minor areas of granular-shaped bainite (GB) were observed along the grain boundaries (Figure 5b). Ferrite grains were pinned by the nano-sized precipitates (shown by the arrows in Figure 5c), which were EDX-identified as a complex Nb-based carbide (Nb,V, Mo)C with an average concentration of 15.50 ± 2.30 wt.% Nb, 1.15 ± 0.31 wt.% V and 0.35 ± 0.08 wt. % Mo. The concentrations of carbide-forming elements (Nb, V, and Mo) in the precipitates are assessed as being lowered because the results were affected by the EDX response of the ferritic matrix surrounding the carbide particles (the latter was confirmed by the presence of the spectra of Si, Mn, Cr, and Fe dissolved in ferrite (Figure 5d)).

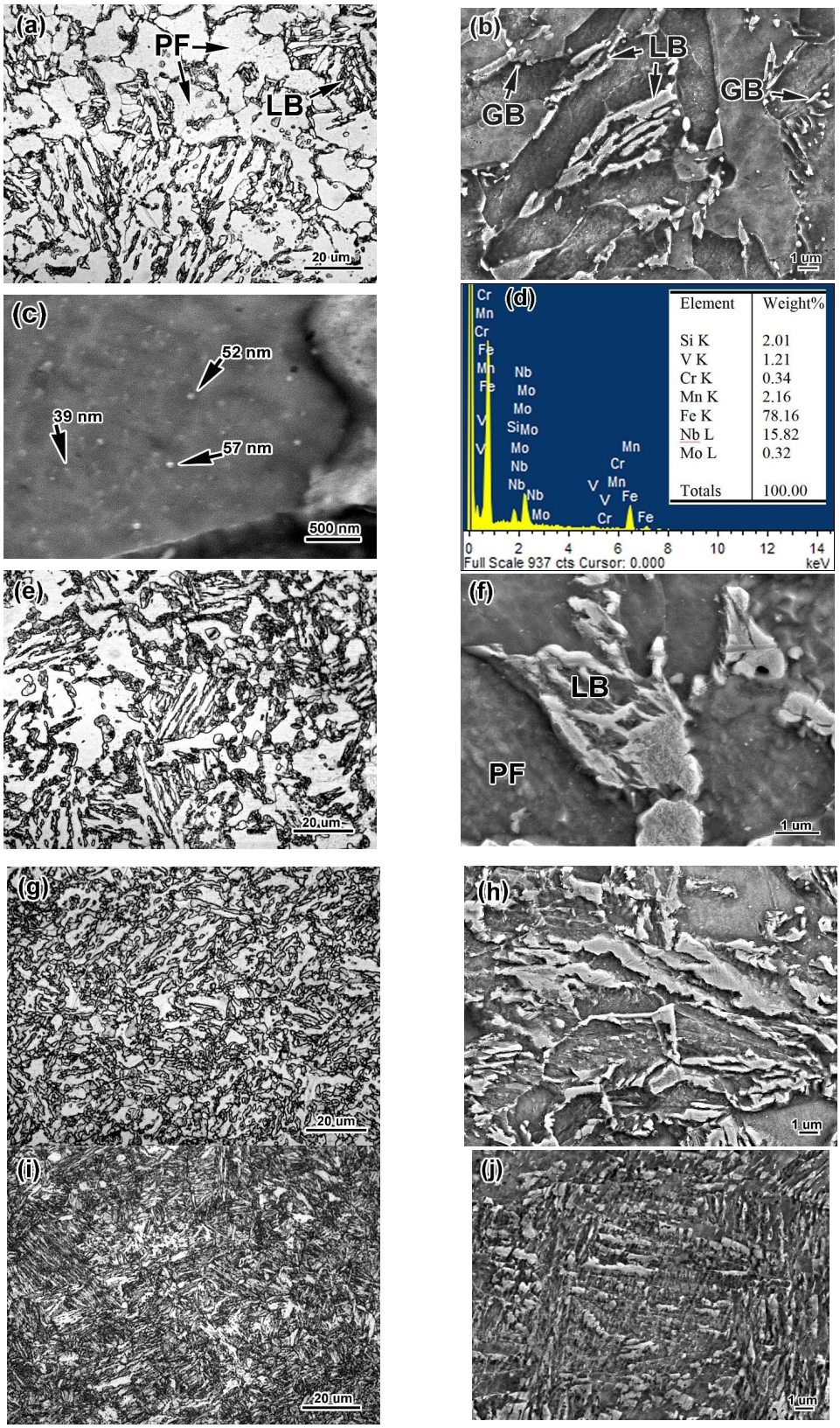

Figure 5. Microstructure of the specimens austenitized at different temperatures: (**a**–**c**) 770 °C, (**d**) EDX-spectrum of a carbide precipitate, (**e**,**f**) 830 °C, (**g**,**h**) 900 °C, and (**i**,**j**) 950 °C ((**a**,**e**,**g**,**i**)—OM images; (**b**–**d**,**f**,**h**,**j**)—SEM images; F—proeutectoid ferrite, LB—lamellar bainite, and GB—granular bainite).

A reduction in the volume fraction of proeutectoid ferrite was observed with a corresponding increase in the bainite amount (Figure 5e,f) as the austenitizing temperature was increased to 830 °C. The volume fraction of proeutectoid ferrite reduced drastically at T_A = 900 °C, and the structure primarily consisted of bainite (Figure 5g) while bainitic laths became shorter (fragmented) and less oriented (Figure 5h). The austenitization in the austenite domain (T_A = 950 °C) resulted in the elimination of a proeutectoid ferrite, and the entire structure consisted of bunches of short parallel (partially fragmented) bainitic plates, as shown in Figure 5i,k.

Figure 6a shows the XRD patterns of the austempered specimens. Each austenitization temperature was characterized by a similar XRD pattern containing the high peaks of α-Fe (bcc) and low peaks of γ-Fe (fcc). The austenitization at 770 °C (Figure 6b) is indicated by the lowest values of the volume fraction of retained austenite (2.48 vol.%) and carbon content in RA (0.82 wt.%). With a austenitization temperature increase to 900 °C, the RA volume fraction gradually increased to 8.65 vol.%. As T_A increased to 950 °C, the RA volume fraction decreased to 5.45 vol.%, which was still twice as high as at T_A = 770 °C. At T_A = 830–950 °C, the carbon content in RA reached 1.18–1.24 wt.%, which is 1.4–1.5 times higher than that at 770 °C.

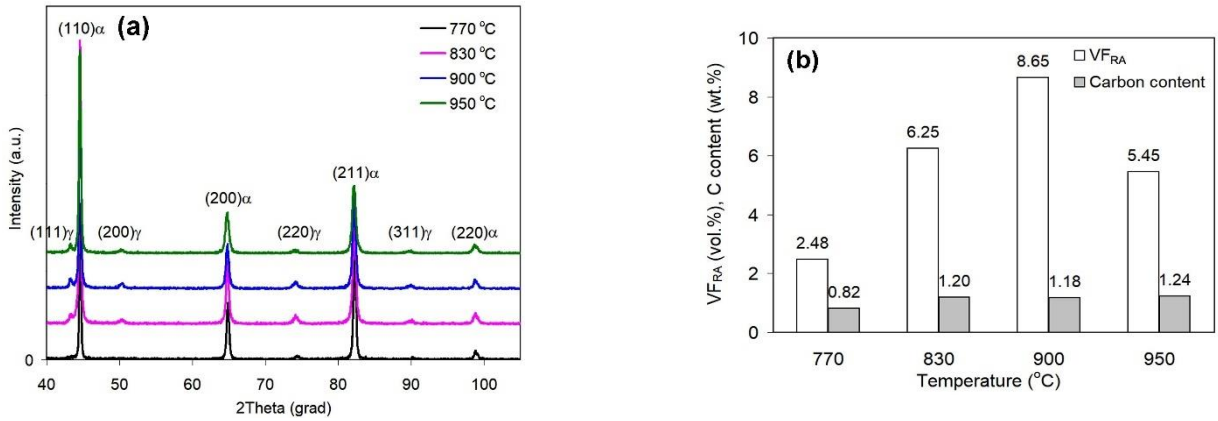

Figure 6. (**a**) XRD patterns of heat-treated specimens and (**b**) effect of austenitizing temperature on the volume fraction of RA and carbon content in RA.

Figures 7 and 8 present the fine structures of heat-treated specimens. Figure 7a illustrates that the bainite in the specimen that was austenitized at 770 °C bainite consisted of elongated α-laths having a width of about 0.68 ± 0.17 μm with occasional austenite interlayers. Dislocation clots and nano-scaled carbide particles were observed inside the laths (Figure 7b). Furthermore, the coarse plate-shaped (of 37.1 ± 8.0 nm width) and grain-shaped (of 112.8 ± 8.4 nm diameter) precipitates were observed between the ferritic laths (Figure 7c). The dark field observation in a cementite reflex (insert to Figure 7b) and the selected area electron diffraction (SAED) pattern confirmed that the precipitates were carbides with an orthorhombic lattice, which is characteristic of the Fe_3C carbide. The presence of cementite within the bainite structure became apparent only after austenitization at 770 °C. The cementite carbides were not present in the fine structure of the specimen austenitized at 830 °C. Instead, a higher amount of RA was detected (Figure 7d) as interlath films (of 80.1 ± 28.8 nm width), which was confirmed by the SAED analysis (Figure 7f). Ferritic laths exhibited a high density of dislocations arranged in the dislocation walls to form the sub-grains, as shown in Figure 7g.

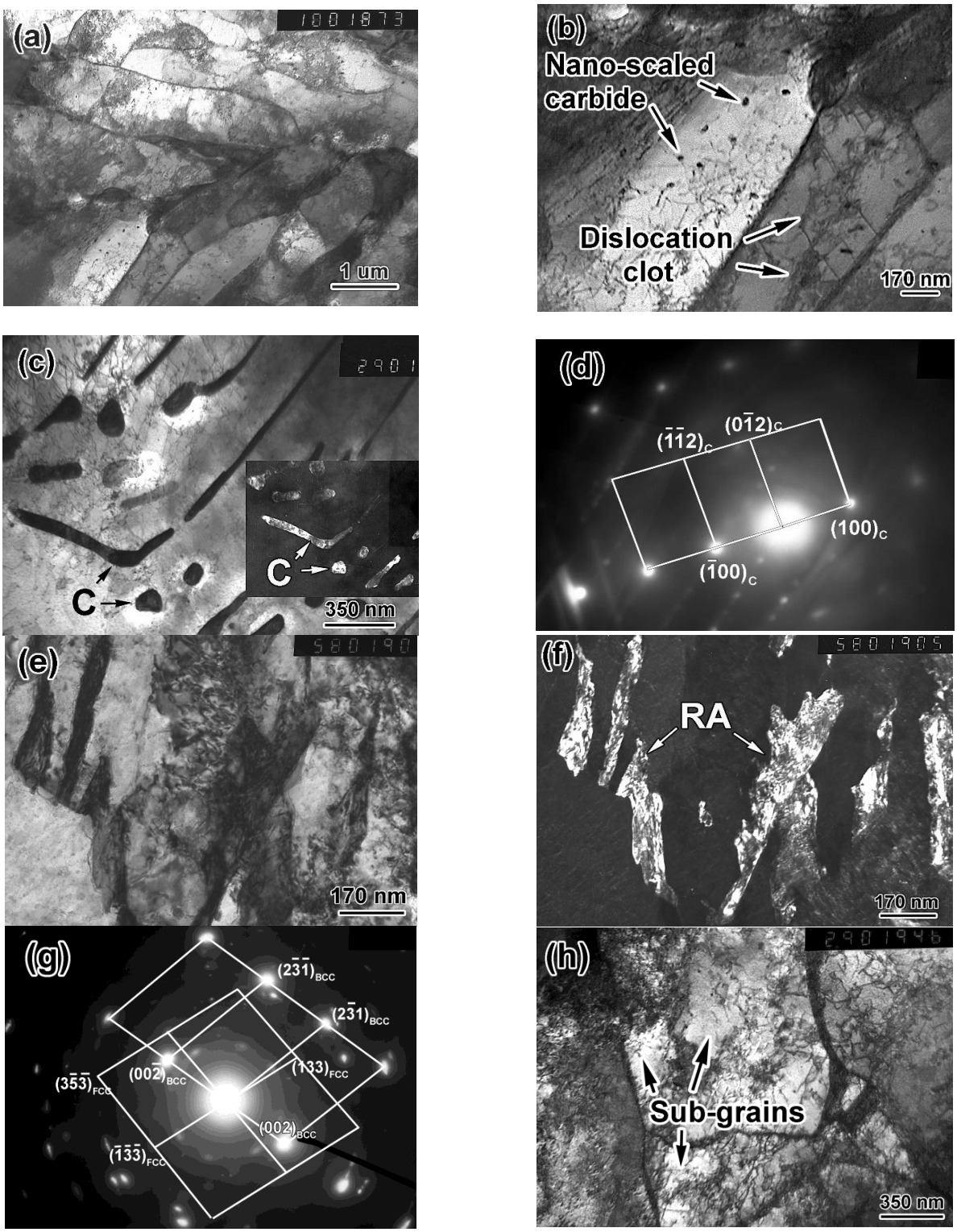

Figure 7. TEM images of the specimens austenitized at 770 °C (**a**–**d**) and 830 °C (**e**–**h**). (**a**) The substructure of bainitic ferrite, (**b**) nano-scaled carbides and dislocation clots, (**c**) the cementite precipitates between the ferrite laths, and the dark-field image in a cementite reflection (insert), (**d**) SAED pattern of (**c**) showing the reflection on the $[0\bar{2}\bar{1}]$ zone axis of cementite, (**e**) bright-field image of ferrite laths and RA films, (**f**) dark-field image of (**d**) in austenite reflection, (**g**) SAED pattern of (**f**) showing the reflection on the [320] zone axis of ferrite and the $[36\bar{7}]$ zone axis of austenite, (**h**) dislocation walls inside the ferrite laths. (C is cementite, BCC is ferrite, and FCC is austenite).

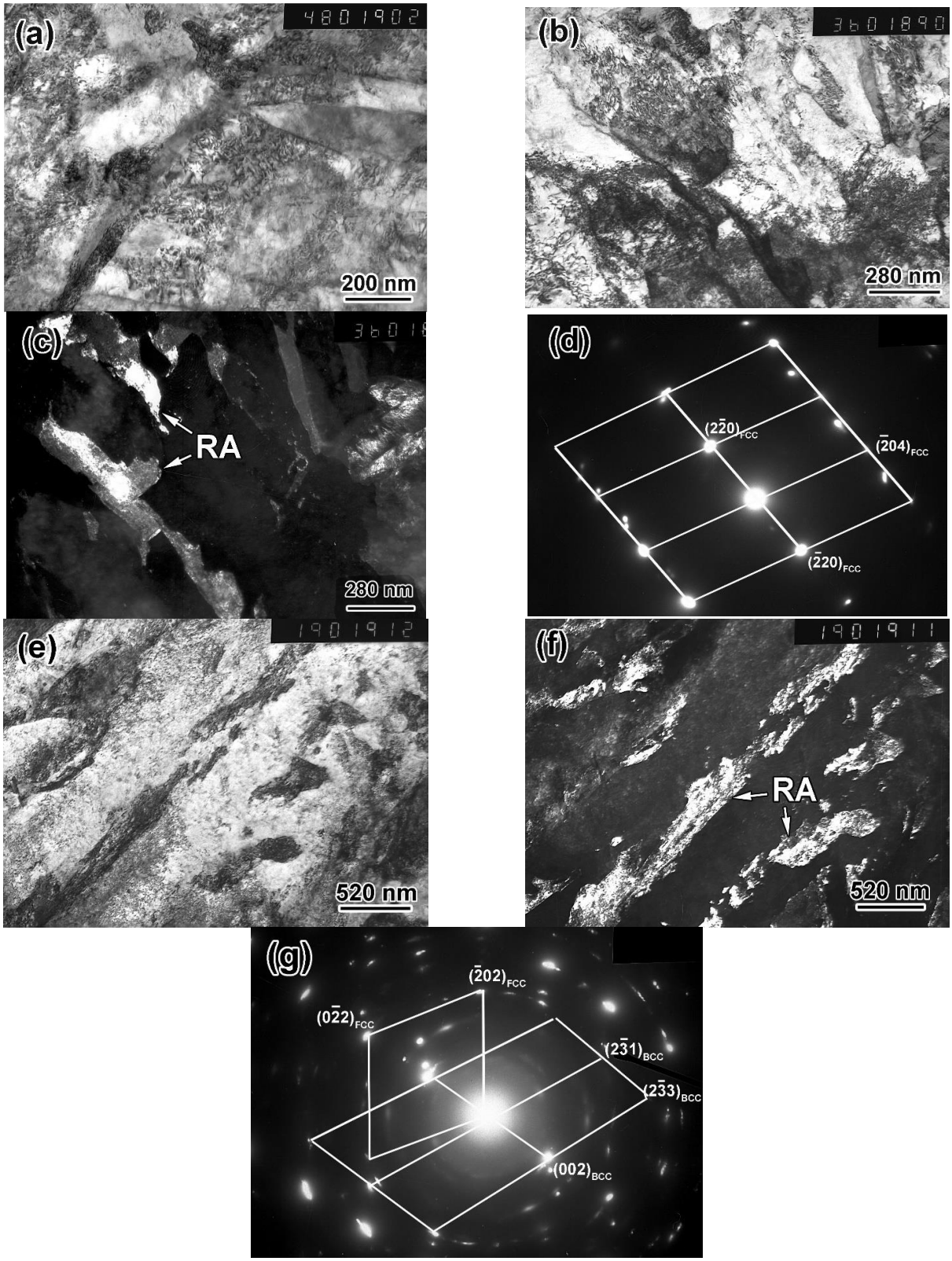

Figure 8. TEM images of the specimens austenitized at 900 °C (**a**–**d**) and 950 °C (**e**–**g**). (**a**) Dislocations in ferrite lath, (**b**) bright-field image of ferrite and RA, (**c**) dark-field image of (**b**) in austenite reflection, (**d**) SAED pattern of (**c**) showing the reflection on the [320] zone axis of ferrite and [114] zone axis of austenite, (**e**) bright-field of ferrite and RA, (**f**) dark-field image of (**e**) in austenite reflection, (**g**) SAED pattern of (**f**) showing the reflection on the [221] zone axis of austenite (FCC).

Figure 8a–d depict the fine structure of the specimen austenized at 900 °C. As shown in Figure 8a, bainitic laths were more blurred due to higher dislocation density at 900 °C. Retained austenite was found to be interlath films with a width of 108.5 ± 34.9 nm, which was higher than that at T_A = 830 °C (Figure 8b–d). The specimen austenitized at 950 °C had the same structural features, while the RA films and occasional bulky areas had a bigger size (158.2 ± 25.9 nm) (Figure 8e–g). No cementite carbides were observed at T_A = 900 °C or T_A = 950 °C.

3.3. Fracture Surface Evaluation

Figure 9 depicts the fractured surfaces of the V-notched specimens after impact toughness testing. As shown in Figure 9a, the ruptured surface of the specimens austenized at T_A = 770 °C exhibits a combination of brittle and ductile areas in approximately equal proportions. The brittle areas were the quasi-cleavage facets with a river pattern, indicating the moderate absorption of impact energy. The areas of ductile rupture consisted of small, stretched dimples in the range of 0.3–3.5 µm in the cross-section. A fractured surface of the specimen (T_A = 830 °C) was preferentially quasi-cleavage with a lower fraction of ductile areas (Figure 9b). As shown in Figure 9c,d, the fracture pattern for T_A = 900–950 °C altered to flat quasi-cleavage facets surrounded by ductile tearing-off areas. In these cases, the area fraction of the dimples was notably higher than that at T = 830 °C, with a more uniform distribution of the dimples over the fracture area. Furthermore, the size of microvoids varied within larger limits, reaching ~10 µm. The presence of different sizes of dimples indicated that the micro-voids merged at higher strains, which is beneficial for the impact toughness [44].

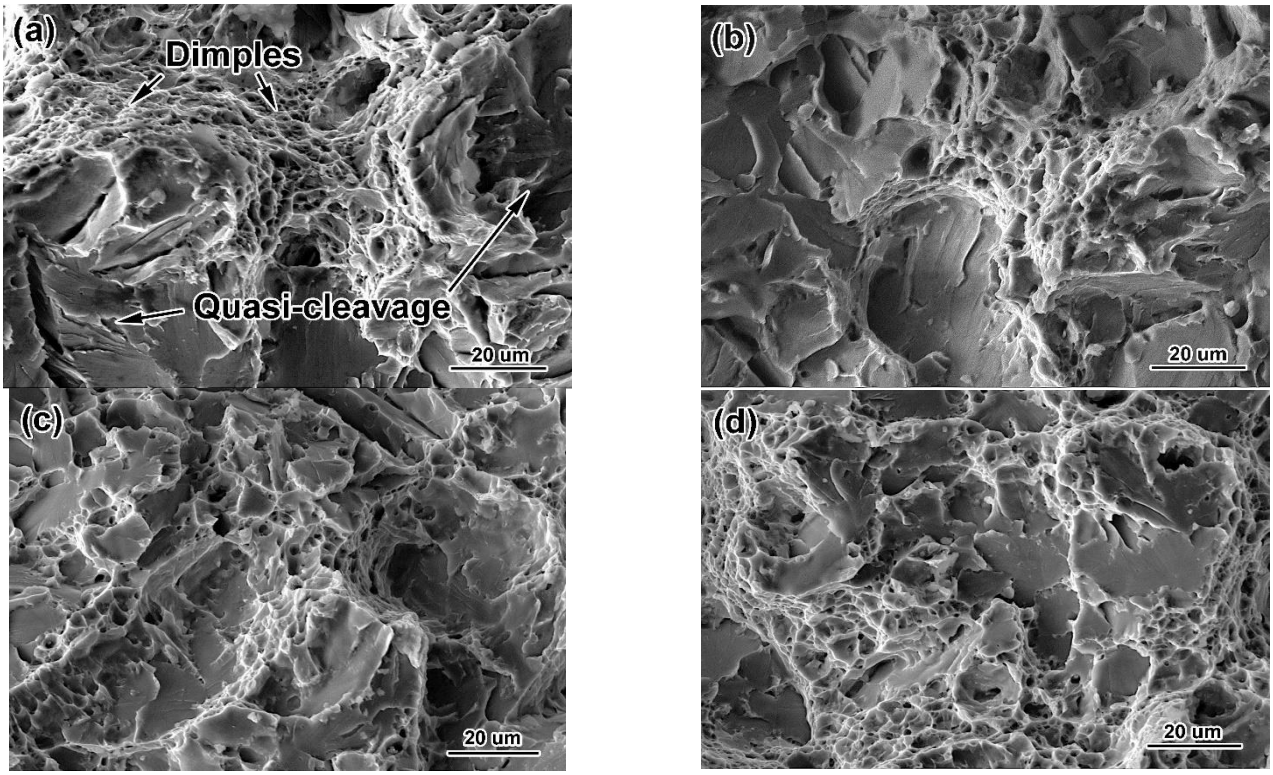

Figure 9. The fracture patterns of the V-notched specimens austenitized at (**a**) 770 °C, (**b**) 830 °C, (**c**) 900 °C, and (**d**) 950 °C.

4. Discussion

The findings of this study demonstrate that the variation in mechanical properties depending on the austenitization temperature does not match the usual trend in which the strength of the steel is inversely proportional to its ductility. As shown in Figure 4, the

strength continuously increases as T_A increases, while the ductility changes nonmonotonically, with the maximum corresponding to T_A = 830 °C. The reason for this behavior is the low ductility at T_A = 770 °C caused by the cementite precipitation during the bainitic transformation. On the one hand, the presence of large carbides along the boundaries between the ferrite laths caused embrittlement of the steel. Furthermore, due to the carbide formation, the gamma-phase was not enriched enough in carbon to ensure the higher amount of retained austenite (RA volume fraction was only about 3 vol.%). Accordingly, during tensile testing, there was no TRIP effect, which could contribute to the ductility and compensate for the brittleness caused by carbide precipitation. At higher austenitization temperatures (830–900 °C), the formation of bainite occurred without the precipitation of carbides, resulting in a sharp increase in the amount of retained austenite. Consequently, despite the lower amount of the soft phase (ferrite) in the structure, the ductility of the steel increased. Thus, an increase in the austenitization temperature modified the mechanism of bainite transformation in steel.

The reason for cementite precipitation was an excessive austenite C-enrichment caused by carbon interphase partitioning during intercritical annealing. The amount of ferrite in the structure reached a maximum (50 vol.%) at 770 °C. Therefore, after the redistribution of carbon its content in austenite was also maximal, which is twice as high as the total content of steel. Additional carbon enrichment of austenite occurs during bainite transformation, which was accompanied by the rejection of carbon into the γ-phase by the growing ferrite plates [45]. To reduce its free chemical energy, carbon-oversaturated austenite discharges into cementite precipitation. Silicon and/or aluminum are usually added to TRIP-assisted steels to prevent this scenario. It is well known that Si and Al suppress the formation of cementite during the tempering of martensite [46]. This effect is typically attributed to the low solubility of Si(Al) in cementite, which implies their diffusion away from the growing carbide particle [47,48]. Another possible reason is that Si increases the coefficient of carbon activity in austenite [49]. When the Si atoms are rejected by the cementite precipitate, a Si-rich zone appears in the matrix near the "matrix/carbide" interphase, where carbon activity is significantly elevated. This may lead to a local increase in free chemical energy, disabling cementite precipitation [50]. Eventually, the amount of retained austenite increases as carbon remains in theγ-phase. The addition of Si(Al) is a basic approach for TRIP-assisted steels, which ensures a desired carbide-free microstructure. In this regard, the question of why it fails in the case of experimental steel arises. The most likely reason for this behavior is alloying of steel with Cr, Mo, and V in an attempt to further improve the mechanical and technological properties of TRIP-assisted steel. As noted above, Cr and Mo were added to increase the hardenability of steel, customizing it for the production of the rolled sheets with heavier sections. Based on the analysis of TTT diagrams (Figure 2), adding Cr and Mo to 0.2%C-Mn-Si TRIP-assisted steel increases the incubation period of austenite→pearlite and austenite→bainite transformations with a corresponding decrease in the critical cooling rate from 600 K/s to 16 K/s (in the pearlite domain) and from 1000 K/s to 227 K/s (in the bainite domain). The critical cooling rate was found to be:

$$V_{crit} = \frac{950 - t_{\min}}{\tau_{\min}}, \quad (1)$$

where t_{min} and τ_{min} are the temperature (°C) and the incubation time (s) corresponding to the "nose" in the TTT diagram.

If the critical cooling rate for the pearlite domain is considered, a rough assessment using the hardenability diagram presented in Reference [51] reveals that the thickness of the sheet, which can be water-cooled to the austempering temperature without causing pearlite formation, increases after adding 0.55 wt.% Cr and 0.20 wt.% Mo eight times (from 6 mm to 48 mm), which is beneficial for industrial applications. This validates the appropriateness of the minor addition of these elements into TRIP-assisted steel. However, Cr, Mo, and V are the elements that promote carbide formation [52]. They reduce carbon activity in austenite (a_C^{γ}) [53,54], thus leveling the inhibiting effect of silicon.

C-rich austenite possesses high free chemical energy that can be reduced by the release of carbon atoms via carbide precipitation. In this case, the decrease in free energy of austenite can be expressed as a difference in the carbon activities $\Delta a_C^\gamma = a_C^\gamma - (a_C^\gamma)'$, where $(a_C^\gamma)'$ is the carbon activity in austenite after the release of the Δ%C amount of carbon. At the same time, the accumulation of silicon at the boundary of the growing carbide increases the carbon activity in austenite ($\Delta a_C^{\gamma Si}$). The cementite inhibition is achieved if a reduction in free energy during the carbide formation is less than an increase in the free energy caused by the silicon effect:

$$\Delta a = \left|\Delta a_C^\gamma\right| - \left|\Delta a_C^{\gamma Si}\right| \leq 0, \tag{2}$$

where Δa is the total change in the free energy of austenite.

Assuming that all carbon is in the solution and taking the "austenite/ferrite" ratio, the carbon content in austenite after carbon redistribution in the intercritical range is roughly estimated as 0.39 wt.% for 770 °C, 0.26 wt.% for 830 °C, and 0.21 wt.% for 900 °C. It is assumed that all this carbon is released from the solution via cementite precipitation during bainite transformation (caused by low C solubility in ferrite). The corresponding change in the activity of carbon in austenite is calculated as [55]:

$$a_C^\gamma = \gamma_C \cdot x_C^\gamma \cdot f_C^i \cdot f_C^{i+1} \cdot \ldots \cdot f_C^n, \tag{3}$$

where γ_c is the carbon activity coefficient in unalloyed austenite,x_C^γ is the carbon mole fraction in austenite, and f_C^i is the coefficient of carbon activity due to the influence of the i-th alloying element.

The parameters of Equation (3) can be found as [55]:

$$a_C^\gamma = \gamma_C \cdot x_C^\gamma \cdot f_C^i \cdot f_C^{i+1} \cdot \ldots \cdot f_C^n, \tag{4}$$

$$\gamma_c = x_c/(1 - 5x_c), \tag{5}$$

$$\ln f_c^{Si} = 10.35 \cdot x_{Si}, \tag{6}$$

$$\ln f_c^{Mm} = \left[-\frac{6500}{T} + 1.45\right] \cdot x_{Mm}, \tag{7}$$

$$\ln f_c^{Cr} = \left[-\frac{21900}{T} + 6.3\right] \cdot x_{Cr}, \tag{8}$$

$$\ln f_c^{Mo} = \left[-\frac{37600}{T} + 16.9\right] \cdot x_{Mo}. \tag{9}$$

where x_{Si}, x_{Mn}, x_{Cr}, and x_{Mo} are the mole fractions of the elements in austenite, and T is the temperature (K).

As shown in Reference [33], due to the partitioning of elements at 770 °C, the contents of Mn, Cr and Si in austenite in the experimental steel were 2.3 wt.%, 0.80 wt.%, and 1.60 wt.%, respectively. The molybdenum content in austenite is roughly taken as 0.1 wt.% (half of its total content in steel) since Mo partitions between the matrix and carbide (Nb, V, Mo)C. The aforementioned values of the element concentration were utilized for the calculations. The effect of vanadium was not considered since V was mostly bound in (Nb, V, Mo)C carbide.

Figure 10 depicts the results of the calculations. The curves in the figure represent the total change in the free energy of austenite (Δa) depending on the Si content. The case of ΔC = 0.4 wt.% C is represented by curves 1 and 2. It is observed that in steel without chromium (curve 1), condition (2) is satisfied when the Si content in the matrix next to the growing carbide is at least 3.2 wt.%. This value exceeds the initial Si content in austenite (1.6 wt.%), necessitating the double silicon accumulation in the matrix before the growing carbide. The experimental evidence of such silicon accumulation was previously reported in References [56,57]. Tu et al. [56] revealed a 1.75-fold Si-enrichment in the matrix next to the interface with cementite carbide in Mn-Si steel. Similar results were

presented in work [57] on white cast iron, which revealed a 2.3-time Si-enrichment in the ferrite regions adjacent to cementite particles. Thus, condition (2) can be achieved in C-Si-Mn TRIP-assisted steel having 1.6 wt.% Si, suggesting that the thermodynamic situation favors cementite inhibition. The addition of Cr and Mo decreases the carbon activity, reducing the inhibiting effect of silicon (illustrated by curve 2, which is higher than curve 1). Consequently, curve 2 reaches the "null" value at about 4.2 wt.% Si, indicating that the total silicon content in steel should exceed 2 wt.% to meet condition (2). Consequently, the thermodynamic equilibrium in steel containing Cr and Mo shifts in favor of carbide precipitation, as observed at T_A = 770 °C.

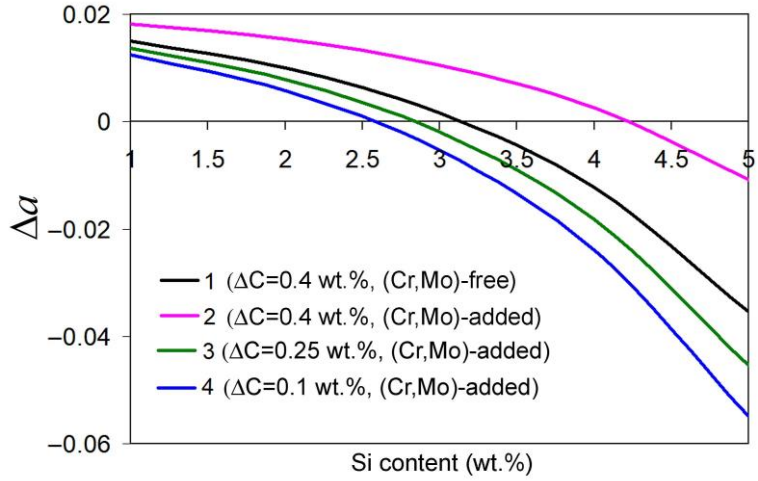

Figure 10. Effect of the Si content on the total change in free energy of austenite caused by cementite precipitation.

Curves 3 and 4 refer to the cases of (Cr,Mo)-added steel with ΔC of 0.25 wt.% and 0.1 wt.%, respectively. They reach the "null" value (condition (2)) at the Si content ≤3.2 wt.%. This indicates that the cementite precipitation in the experimental steel can be suppressed at a lower amount of released carbon. Therefore, to change the resultant structure from "ferrite/cementite" to "carbide-free bainite/RA", the carbon content in austenite before the austempering should be lower at least by 1.5 times (i.e., 0.25 wt.%). This requires decreasing the quantity of proeutectoid ferrite from 50 vol.% (at 770 °C) to 25 vol.% (at 830 °C), which correspondingly lowers the carbon enrichment of austenite. Despite the diminishing of proeutectoid ferrite, austenitization at 830 °C led to maximum ductility (25%) due to the absence of coarse cementite and an increased amount of retained austenite (as thin films). A significant drop in TEL occurred only at T_A = 950 °C (single γ phase domain), which was associated with the full elimination of proeutectoid ferrite and a decrease in the RA volume fraction.

In contrast to TEL, impact toughness was controlled by the amount of soft phases (ferrite, RA) rather than cementite precipitation. At T_A = 770 °C, the impact toughness was high enough (105 J/cm^2), despite the presence of coarse cementite precipitates. The detrimental effect of the precipitates was compensated by a high volume fraction of ductile proeutectoid ferrite. Despite the absence of cementite and enhanced RA amount, a 1.5-times drop in the ferrite amount at T_A = 830 °C resulted in a 20% reduction in impact toughness. The impact toughness increased to 95 J/cm^2 at T_A = 900 °C due to the maximum volume fraction of retained austenite. Unexpectedly, the highest impact toughness value (113 J/cm^2) was attributed to T_A = 950 °C when the amount of ductile structural components (ferrite, RA) decreased to minimal level. This result was due to the absence of localized stress that appears at the "bainite lath/ferrite" boundary as a consequence of the differences in specific volumes of bainitic ferrite and proeutectoid ferrite [58]. Furthermore, the austenitization at 950 °C leveled the concentration of elements in austenite, thus increasing strain and

fracture homogeneity, which was evidenced by a more uniform allocation of ductile areas on the fractured surface (Figure 8c).

Analysis of the strain hardening rate (SHR) provides an important insight into the steel tensile behavior. SHR is calculated as SHR = $d\sigma/d\varepsilon$, where σ is the true stress and ε is the true strain (TS) [59]. Figure 11 displays the TS and SHR curves for different austenitizing temperatures. For all the austenitizing temperatures a sharp rising of SHR at the initial strain stage (ε = 0.005−0.01) was followed by a decrease in the SHR value at up to ε∼0.025, which is attributed to the cumulative interactions of gliding dislocations followed by the blocking of the close-packed plains of their gliding [59,60]. The next strain stage was characterized by an increase in the SHR, indicating a strain hardening phenomenon [61]. It is observed that the SHR curves for T_A = 770 °C and T_A = 830 °C exhibited similar behavior, with a minor hardening effect lasting up to the strain of about 0.05. The specimens austenitized at 900 °C and 950 °C showed a significantly higher strain hardening that lasted to the higher strain. The most extended strain hardening was noted for T_A = 950 °C, where the maximum SHR corresponded to a strain of nearly 0.13.

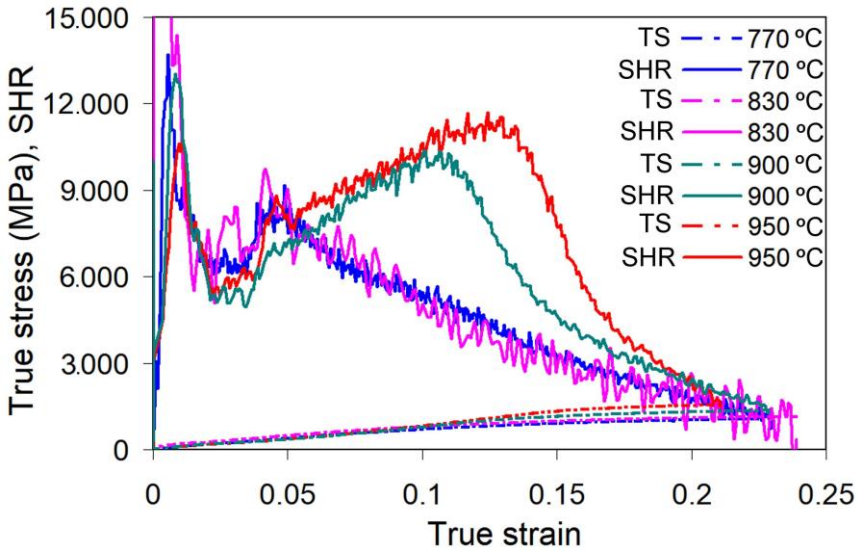

Figure 11. The curves of true strain (TS) and SHR for the specimens depending on the austenitizing temperature.

The difference in SHR behavior can be explained based on the ferrite volume fraction and the degree of the TRIP effect progress. The proeutectoid ferrite was the phase where the deformation of the specimens austenitized at 770–830 °C started and developed. Ferrite exhibited a modest ability to strain hardening, which only corresponded to low strain. Due to the low amount of RA (at T_A = 770 °C), or presumably due to its high stability to SIMT (at T_A = 830 °C), RA did not contribute much to the strain hardening. At T_A = 900–950 °C the amount of ferrite was negligible, and therefore deformation started in RA and later involved bainitic ferrite. The higher strain hardening at T_A = 900–950 °C was related to a more apparent manifestation of the TRIP effect [59], which can be explained by an increase in the RA volume fraction (maximal at T_A = 900 °C) or by an increase in austenite's susceptibility to strain-induced martensite transformation (SIMT), which is presumably maximal at T_A = 950 °C. One can presume that T_A promotes the increase in the RA metastability due to a decrease in manganese content in austenite during intercritical annealing. The austenite's metastability to SIMT is strongly dependent on its chemical composition, as described by Angel's equation [62]:

$$M_{d30} = 413 - 462(C + N) - 9.2(Si) - 8.1(Mn) - 13.7(Cr) - 9.5(Ni) - 18.5(Mo) \quad (10)$$

where M_{d30} is the temperature that refers to the 50 vol.% of martensite formed at 30% true strain; C, N, Si, Mn, Cr, Ni, and Mo are the contents of the chemical elements (wt.%).

As seen in Equation (10), manganese lowers the Md_{30} temperature, thus inhibiting SIMT. During intercritical annealing, Mn was partitioned to austenite and, eventually, its content in the γ-phase was increased by 1.3-times at 770 °C relative to its nominal concentration in steel [33]. An increased Mn content was inherited by retained austenite, resulting in its higher stability to SIMT. However, with a T_A increase, the amount of Mn in austenite gradually decreased, facilitating the austenite's propensity to SIMT. Accordingly, strain-hardening rate increased as well. The most intensive strain-hardening was observed at T_A = 950 °C which is attributed to the highest metastability of RA to a the strain-induced martensitic transformation. However, it might adversely affect ductility, as indicated by the minimum TEL value noted for T_A = 950 °C.

Area reduction characterizes the metal's ductility under tensile strain related to the necking formation at the stage of non-uniform deformation. The AR value is dependent on the steel ductility/brittleness or on the kinetics of the TRIP effect (the strain-induced martensite strengthening delays the necking formation [1,12]). These factors can be used to explain the gradual AR increase with the austenitization temperature increasing (Figure 4). The specimens austenized at 770 °C had the lowest AR value (33%) due to the high brittleness caused by coarse cementite precipitates in the bainite areas (Figure 7c). Preventing cementite formation and the appearance of retained austenite led to an AR increase to 44% at T_A = 830 °C. The maximal amount of ductile retained austenite gained at T_A = 900 °C resulted in even higher AR (51%). The highest AR value (62%) at T_A = 950 °C was presumably caused by the same structural factor that ensured the highest impact toughness at this austenitization temperature (formulated above). It should be noted that TRIP effect development in the specimens austenitized at T_A = 900–950 °C did not result in inhibiting the neck formation because of the relatively low RA volume fraction in their structure.

The study showed that the austenitization at 900 °C provided the best combination of the mechanical properties of the examined steel: UTS of 1040 MPa, TEL of 23%, KCV of 95 J/cm^2, and PSE of 23.9 GPa·%. This was ensured by the optimal structure consisting of carbide-free bainite (∼86 vol.%), RA (∼9 vol.%), and proeutectoid ferrite (∼5 vol.%). This structure demonstrated a moderate propensity to SIMT, which is beneficial for preventing early embrittlement and fracture [63]. The findings demonstrated that the optimal "ferrite/austenite" ratio for the examined Cr(Mo)-alloyed steel before the austempering holding is significantly lower than that previously reported for the C-Si-Mn TRIP-assisted steels, where a volume fraction of ferrite of about 50 vol.% was recommended [64,65]. A low amount of proeutectoid ferrite prevents the excessive carbon-enrichment of austenite that may provoke cementite precipitation during austenite→bainite transformation. In our case, the optimum austenitizing temperature is close to the Ac_3 point. Similar results were reported by Sugimoto and Srivastava [15], who proposed the heat treatment of C-Si-Mn-1 wt.% Cr TRIP-added steel with austenitization at a temperature above the Ac_3 point. Given the possibility of alloying elements influencing the mechanism of bainite transformation an alternative approach for the austempering process for the Cr(Mo)-alloyed TRIP-assisted steel should be applied.

5. Conclusions

In the present work, the effect of the temperature of intercritical annealing on the structure and mechanical properties of the (Cr,Mo, and V)-alloyed TRIP-assisted steel, which is subjected to austempering at 350 °C, was investigated. The main conclusions are as follows:

1. With an increase in the austenitization temperature, the volume fraction of proeutectoid ferrite decreased from 50 vol.% (at T_A = 770 °C) to 0 vol.% (at T_A = 950 °C), followed by a monotonous increase in UTS from 821 MPa to 1207 MPa. Total elongation changed along a curve with a maximum (25%) associated with austenitization at 830 °C. Furthermore, this temperature corresponded to the lowest impact toughness.
2. When steel was austenitized at 770 °C, the bainitic transformation proceeded through the precipitation of coarse cementite carbides, leading to lowered ductility and a

minimum amount of RA (2.5 vol.%). At higher austenitization temperatures, carbide-free bainite was formed with a 2.5–3.5 times increase in the RA volume fraction (to 5.5–8.5 vol.%) and 1.5 times increase in the concentration of carbon in RA.

3. The optimal temperature of intercritical annealing was determined to be 900 °C, which, after austempering, resulted in a structure consisting of carbide-free bainite (∼86 vol.%), retained austenite (RA) (∼9 vol.%), and proeutectoid ferrite (∼5 vol.%). Here, RA exhibited a moderate tendency to strain-induced martensite transformation. Furthermore, this structure ensured an advanced combination of mechanical properties (UTS of 1040 MPa, TEL of 23%, KCV of 95 J/cm^2, and PSE of 23.9 GPa·%).
4. The addition of Cr and Mo into C-Si-Mn TRIP-assisted steel promotes cementite formation during austempering holding by decreasing the coefficient of carbon activity in austenite. This adversely affects the mechanical properties of the steel. Therefore, it is crucial to employ an alternative approach to select the intercritical annealing temperature. This strategy involves decreasing the volume fraction of proeutectoid ferrite to prevent excessive carbon enrichment of austenite before the austempering holding.

Author Contributions: Conceptualization, V.Z., V.E., M.D.; methodology, V.E., M.D., K.W., F.K., I.P.; software, M.F.; validation, M.B., V.P.; formal analysis, Y.C., M.B.; investigation, V.Z., I.P., M.B., V.P., M.F., Y.C.; resources, I.P., K.W.; data curation, V.P.; writing—original draft preparation, V.Z., V.E., I.P., M.B.; writing—review and editing, V.Z., V.E., I.P., M.D., K.W., F.K.; visualization, V.Z., M.B.; supervision, V.E.; project administration, Y.C.; funding acquisition, I.P, V.E, K.W. All authors have read and agreed to the published version of the manuscript.

Funding: This research was funded by the Ministry of Education and Science of Ukraine within project No 0120U102087 and by Slovak Research and Development Agency within the Slovak-Ukrainian project APVV-SK-UA-21-0023 (No 0122U200119).

Acknowledgments: V. Zurnadzhy and V. Efremenko acknowledge the partial financial support of the Ministry of Education and Science of Ukraine in the frame of project No. 0122U200120.

Conflicts of Interest: The authors declare no conflict of interest.

References

1. Bleck, W.; Guo, X.; Ma, Y. The TRIP effect and its application in cold formable sheet steels. *Steel Res. Int.* **2019**, *88*, 1700218. [CrossRef]
2. Guo, R.; Zhou, J.; Shi, Y. Application of the high strength steel in the automobile. *Adv. Mater. Res.* **2013**, *748*, 227–230. [CrossRef]
3. Zhang, Y.; Ma, Y.; Kang, Y.; Yu, H. Mechanical properties and microstructure of TRIP steels produced using TSCR process. *J. Univ. Sci. Technol. Beijing* **2006**, *13*, 416–419. [CrossRef]
4. Sugimoto, K.; Iida, T.; Sakaguchi, J.; Kashima, T. Retained austenite characteristics and tensile properties in a TRIP type bainitic sheet steel. *ISIJ Int.* **2000**, *40*, 902–908. [CrossRef]
5. Injeti, V.S.Y.; Li, Z.C.; Yu, B.; Misra, R.D.K.; Cai, Z.H.; Ding, H. Macro to nanoscale deformation of transformation-induced plasticity steels: Impact of aluminum on the microstructure and deformation behavior. *J. Mater. Sci. Technol.* **2018**, *34*, 745–775. [CrossRef]
6. Sakuma, Y.; Matsumura, O.; Takechi, H. Mechanical properties and retained austenite in intercritically heat-treated bainite-transformed steel and their variation with Si and Mn additions. *Metall. Mater. Trans. A* **1991**, *22*, 489–498. [CrossRef]
7. He, Z.; Liu, H.; Zhu, Z.; Zheng, W.; He, Y.; Li, L. Quantitative Description of external force induced phase transformation in silicon–manganese (Si–Mn) transformation induced plasticity (TRIP) steels. *Materials* **2019**, *12*, 3781. [CrossRef]
8. Girault, E.; Mertens, A.; Pascal, J.; Houbaert, Y.; Verlinden, B.; Humbeeck, J. Comparison of the effects of silicon and aluminium on the tensile behaviour of multiphase TRIP-assisted steels. *Scr. Mater.* **2001**, *44*, 885–892. [CrossRef]
9. Lee, K.; Ryu, J.H.; Lee, S.W.; Lee, W.H.; Kim, J.I.; Suh, D.-W. Influence of the initial microstructure on the heat treatment response and tensile properties of TRIP-assisted steel. *Metall. Mater. Trans. A* **2016**, *47*, 5259–5265. [CrossRef]
10. Ennis, B.L.; Jimenez-Melero, E.; Atzem, E.H.; Krugl, M.; Azeem, M.A.; Rowley, D.; Daisenberger, D.; Hanlon, D.N.; Lee, P.D. Metastable austenite driven work-hardening behaviour in a TRIP-assisted dual phase steel. *Int. J. Plast.* **2017**, *88*, 126–139. [CrossRef]
11. Sohn, S.S.; Song, H.; Kwak, J.-H.; Lee, S. Dramatic improvement of strain hardening and ductility to 95% in highly-deformable high-strength duplex lightweight steels. *Sci. Rep.* **2017**, *7*, 1927. [CrossRef] [PubMed]
12. Cheiliakh, O.P.; Cheiliakh, Y.O. Implementation of physical effects in the operation of smart materials to form their properties. *Usp. Fiz. Met.* **2020**, *21*, 363–463. [CrossRef]
13. Malinov, L.S.; Malysheva, I.E.; Klimov, E.S.; Kukhar, V.V.; Balalayeva, E.Y. Effect of particular combinations of quenching, tempering and carburization on abrasive wear of low-carbon manganese steels with metastable austenite. *Mater. Sci. Forum* **2019**, *945*, 574–578. [CrossRef]

14. Shen, Y.F.; Qiu, L.N.; Sun, X.; Zuo, L.; Liaw, P.K.; Raabe, D. Effects of retained austenite volume fraction, morphology, and carbon content on strength and ductility of nanostructured TRIP-assisted steels. *Mater. Sci. Eng. A* **2015**, *636*, 551–564. [CrossRef]
15. Sugimoto, K.; Srivastava, A.K. Microstructure and mechanical properties of a TRIP-aided martensitic steel. *Metallogr. Microstruct. Anal.* **2015**, *4*, 344–354. [CrossRef]
16. Tang, S.; Lan, H.; Li, J.; Liu, Z.; Wang, G. The Role of Microstructural constituents on strength–ductility–local formability of a transformation-induced plasticity-aided bainitic steel. *Steel Res. Int.* **2021**, *92*, 2000474. [CrossRef]
17. Koval', A.D.; Efremenko, V.G.; Brykov, M.N.; Andrushchenko, M.I.; Kulikovskii, R.A.; Efremenko, A.V. Principles for developing grinding media with increased wear resistance. Part 1. Abrasive wear resistance of iron-based alloys. *J. Frict. Wear* **2012**, *33*, 39–46. [CrossRef]
18. Hesse, O.; Merker, J.; Brykov, M.; Efremenko, V. Zur Festigkeit niedriglegierter Stähle mit erhöhtem Kohlenstoffgehalt gegen abrasiven Verschleiß. *Tribologie und Schmierungstechnik* **2013**, *60*, 37–43.
19. Song, C.; Wang, H.; Sun, Z.; Wei, Z.; Chen, H.; Wang, Y.; Lu, J. Effect of multiphase microstructure on fatigue crack propagation behavior in TRIP-assisted steels. *Int. J. Fatigue* **2020**, *133*, 105425. [CrossRef]
20. Rykavets, Z.M.; Bouquerel, J.; Vogt, J.-B.; Duriagina, Z.A.; Kulyk, V.V.; Tepla, T.L.; Bohun, L.I.; Kovbasyuk, T.M. Investigation of the microstructure and properties of TRIP 800 steel subjected to low-cycle fatigues. *Usp. Fiz. Met.* **2019**, *20*, 620–633. [CrossRef]
21. Oja, O.; Saastamoinen, A.; Patnamsetty, M.; Honkanen, M.; Peura, P.; Järvenpää, M. Microstructure and mechanical properties of Nb and V microalloyed TRIP-assisted steels. *Metals* **2019**, *9*, 887. [CrossRef]
22. Abbasi, E.; Rainforth, M. Microstructural evolution of Nb–V–Mo and V containing TRIP-assisted steels during thermomechanical processing. *J. Mater. Sci. Technol.* **2017**, *33*, 311–320. [CrossRef]
23. Krizan, D.; De Cooman, B.C. Mechanical properties of TRIP Steel microalloyed with Ti. *Metall. Mater. Trans. A* **2014**, *45*, 3481–3492. [CrossRef]
24. Mohrbacher, H.; Yang, J.-R.; Chen, Y.-W.; Rehrl, J.; Hebesberger, T. Effect of Nb and Mo additions in the microstructure/tensile property relationship in high strength quenched and quenched and tempered boron steels. *Metals* **2020**, *10*, 504. [CrossRef]
25. Abbasi, E.; Rainforth, W.M. Effect of Nb-Mo additions on precipitation behaviour in V microalloyed TRIP-assisted steels. *Mater. Sci. Technol.* **2016**, *32*, 1721–1729. [CrossRef]
26. Kučerová, L.; Bystrianský, M. The effect of chemical composition on microstructure and properties of TRIP steels. *J. Achiev. Mater. Manuf. Eng.* **2016**, *77*, 5–12. [CrossRef]
27. Kim, S.-J.; Lee, C.G.; Lee, T.-H.; Oh, C.-S. Effect of Cu, Cr and Ni on mechanical properties of 0.15 wt.% C TRIP-aided cold rolled steels. *Scr. Mater.* **2003**, *48*, 539–544. [CrossRef]
28. Zinsaz-Borujerdi, A.; Zarei-Hanzaki, A.; Abedi, H.R.; Karam-Abian, M.; Ding, H.; Han, D.; Kheradmand, N. Room temperature mechanical properties and microstructure of a low alloyed TRIP-assisted steel subjected to one-step and two-step quenching and partitioning process. *Mater. Sci. Eng. A* **2018**, *725*, 341–349. [CrossRef]
29. Sukhova, O.V. The effect of carbon content and cooling rate on the structure of boron-rich Fe–B–C alloys. *Phys. Chem. Solid State* **2020**, *21*, 355–360. [CrossRef]
30. Jacques, P.; Girault, E.; Catlin, T.; Geerlofs, N.; Kop, T.; van der Zwaag, S.; Delannay, F. Bainite transformation of low carbon Mn–Si TRIP-assisted multiphase steels: Influence of silicon content on cementite precipitation and austenite retention. *Mater. Sci. Eng. A* **1999**, *273–275*, 475–479. [CrossRef]
31. Lee, S.-J.; Lee, S.; De Cooman, B.C. Mn partitioning during the intercritical annealing of ultrafine-grained 6% Mn transformation-induced plasticity steel. *Scr. Mater.* **2011**, *64*, 649–652. [CrossRef]
32. Hu, B.; Luo, H. A novel two-step intercritical annealing process to improve mechanical properties of medium Mn steel. *Acta Mater.* **2019**, *176*, 250–263. [CrossRef]
33. Efremenko, V.; Kussa, R.; Petryshynets, I.; Shimizu, K.; Kromka, F.; Zurnadzhy, V.; Gavrilova, V. Element partitioning in low-carbon Si2Mn2CrMoVNb trip-assisted steel in intercritical temperature range. *Acta Metall. Slovaca* **2020**, *26*, 116–121. [CrossRef]
34. Zurnadzhy, V.I.; Efremenko, V.G.; Petryshynets, I.; Shimizu, K.; Brykov, M.N.; Kushchenko, I.V.; Kudin, V.V. Mechanical properties of carbide-free lower bainite in complex-alloyed constructional steel: Effect of bainitizing treatment parameters. *Kov. Mater.* **2020**, *58*, 129–140. [CrossRef]
35. Franceschi, M.; Pezzato, L.; Settimi, A.G.; Gennari, C.; Pigato, M.; Polyakova, M.; Konstantinov, D.; Brunelli, K.; Dabalà, M. Effect of different austempering heat treatments on corrosion properties of high silicon steel. *Materials* **2021**, *14*, 288. [CrossRef]
36. Zurnadzhy, V.I.; Efremenko, V.G.; Wu, K.M.; Petryshynets, I.; Shimizu, K.; Zusin, A.M.; Brykov, M.N.; Andilakhai, V.A. Tailoring strength/ductility combination in 2.5 wt% Si-alloyed middle carbon steel produced by the two-step QP treatment with a prolonged partitioning stage. *Mater. Sci. Eng. A* **2020**, *791*, 139721. [CrossRef]
37. Jacques, P.J.; Delannay, F. Ladrière On the influence of interactions between phases on the mechanical stability of retained austenite in transformation-induced plasticity multiphase steels. *Metall. Mater. Trans. A* **2001**, *32*, 2759–2768. [CrossRef]
38. Fu, B.; Yang, W.Y.; Li, L.F.; Sun, Z.Q. Effect of bainitic transformation temperature on the mechanical behavior of cold-rolled TRIP steels studied with in-situ high-energy X-ray diffraction. *Mater. Sci. Eng. A* **2014**, *603*, 134–140. [CrossRef]
39. Guzmán, A.; Monsalve, A. Effect of bainitic isothermal treatment on the microstructure and mechanical properties of a CMnSiAl TRIP steel. *Metals* **2022**, *12*, 655. [CrossRef]
40. Kurdjumov, G.V.; Utevskyi, L.M.; Entin, R.I. *The Transformations in Iron and Steel*; Nauka: Moscow, Russia, 1977. (In Russian)

41. Garcia-Mateo, C.; Caballero, F.G.; Sourmail, T.; Kuntz, M.; Cornide, J.; Smanio, V.; Elvira, R. Tensile behaviour of a nanocrystalline bainitic steel containing 3 wt% silicon. *Mater. Sci. Eng. A* **2012**, *549*, 185–192. [CrossRef]
42. Kussa, R.; Zurnadzhy, V.; Dabala, M.; Franceschi, M.; Efremenko, V.; Petryshynets, I.; Kromka, F.; Brykov, M. Comparative study on the effect of (Cr, Mo, V)-alloying on transformation and mechanical behavior of 0.2 wt.% C TRIP-assisted steel. *Kov. Mater.* **2022**, *60*, 31–43. [CrossRef]
43. Zurnadzhy, V.I.; Efremenko, V.G.; Wu, K.M.; Lekatou, A.G.; Shimizu, K.; Chabak, Y.G.; Zotov, D.S.; Dunayev, E.V. Quenching and partitioning–based heat treatment for rolled grinding steel balls. *Metall. Mater. Trans. A* **2020**, *51*, 3042–3053. [CrossRef]
44. Zare, A.; Ekrami, A. Influence of martensite volume fraction on tensile properties of triple phase ferrite–bainite–martensite steels. *Mater. Sci. Eng. A* **2011**, *530*, 440–445. [CrossRef]
45. Fadel, A.; Radovic, N.; Glišić, D.; Drobnjak, D. Intragranular ferrite morphologies in medium carbon vanadium-micro alloyed steel. *J. Min. Metall. Sect. B Metall.* **2013**, *49*, 237–244. [CrossRef]
46. Bhadeshia, H.K.D.H.; Edmonds, D.V. The bainite transformation in a silicon steel. *Metall. Trans.* **1979**, *10A*, 895–907. [CrossRef]
47. Edmonds, D.V.; He, K.; Rizzo, K.; De Cooman, B.C.; Matlock, D.K.; Speer, J.G. Quenching and partitioning martensite—A novel steel heat treatment. *Mater. Sci. Eng. A* **2006**, *438*, 25–34. [CrossRef]
48. Barnard, S.J.; Smith, G.D.W.; Garratt-Reed, A.J.; Vander Sande, J. *Advances in the Physical Metallurgy and Applications of Steels*; TMS: London, UK, 1982.
49. Koyama, T.; Kubota, M.; Yoshida, S. Effect of Si concentration on carbon concentration in surface layer after gas carburizing. *ISIJ Int.* **2016**, *56*, 1638–1645. [CrossRef]
50. Million, B.; Kučera, J.; Michalička, P. The influence of silicon on carbon redistribution in steel weldments. *Mater. Sci. Eng. A* **1995**, *190*, 247–252. [CrossRef]
51. Lakhtin, Y.M.; Rakhshtadt, A.G. *Heat Treatment in Machine Building*; Mashine Building: Moscow, Russia, 1980.
52. Chabak, Y.G.; Fedun, V.I.; Shimizu, K.; Efremenko, V.G.; Zurnadzhy, V.I. Phase-structural composition of coating obtained by pulsed plasma treatment using eroded cathode of T1 high speed steel. *Probl. At. Sci. Technol.* **2016**, *104*, 100–106.
53. Wada, T.; Wada, H.; Elliott, J.F.; Chipman, J. Activity of carbon and solubility of carbides in the FCC Fe-Mo-C, Fe-Cr-C, and Fe-V-C alloys. *Metall. Trans.* **1972**, *3*, 2865–2872. [CrossRef]
54. Lobo, J.A.; Geiger, G.H. Thermodynamics of carbon in austenite and Fe-Mo austenite. *Metall. Trans. A* **1976**, *7*, 1359–1364. [CrossRef]
55. Mogutnov, B.M.; Tomilin, I.A.; Shvarzman, L.A. *Thermodynamics of Iron-Based Alloys*; Metallurgija: Moskva, Russia, 1984. (In Russian)
56. Tu, Y.; Huang, L.; Zhang, Q.; Zhou, X.; Jiang, J. Effect of Si on the partitioning of Mn between cementite and ferrite. *Mater. Sci. Technol.* **2017**, *34*, 780–785. [CrossRef]
57. Tkachenko, F.K. On the issue of the effect of silicon on the graphitization of industrial white cast iron. *Izv. Vuzov. Ferr. Metall.* **1959**, *10*, 131–138.
58. Kumar, A.; Dutta, A.; Makineni, S.K.; Herbig, M.R.; Petrov, H.; Sietsma, J. In-situ observation of strain partitioning and damage development in continuously cooled carbide-free bainitic steels using micro digital image correlation. *Mater. Sci. Eng. A* **2019**, *757*, 107–116. [CrossRef]
59. Zhang, B.; Du, L.X.; Dong, Y.; Han, D.X.; Wu, H.Y.; Lu, F.H.; Misra, R.D.K. Structure-property relationship in novel low carbon hot-rolled TRIP steels via thermo-mechanical controlled processing and coiling. *Mater. Sci. Eng. A* **2020**, *771*, 138643. [CrossRef]
60. Vasylyev, M.O.; Mordyuk, B.M.; Voloshko, S.M.; Zakiyev, V.I.; Burmak, A.P.; Pefti, D.V. Hardening of surface layers of Cu–39Zn–1Pb brass at holding and high-frequency impact deformation in liquid nitrogen. *Metallofiz. Noveishie Tekhnol.* **2019**, *41*, 1499–1517. [CrossRef]
61. Chabak, Y.; Efremenko, B.; Petryshynets, I.; Efremenko, V.; Lekatou, A.G.; Zurnadzhy, V.; Bogomol, I.; Fedun, V.; Koval', K.; Pastukhova, T. Structural and tribological assessment of biomedical 316 stainless steel subjected to pulsed-plasma surface modification: Comparison of LPBF 3D printing and conventional fabrication. *Materials* **2021**, *14*, 7671. [CrossRef]
62. Horn, R.M.; Gordon, G.M.; Ford, F.P.; Cowan, R.L. Experience and assessment of stress corrosion cracking in L-grade stainless steel BWR internals. *Nucl. Eng. Des.* **1997**, *147*, 313–325.
63. Gao, G.; Bai, B.; Zhang, H.; Gui, X.; Tan, Z.; Weng, Y. Enhanced TRIP effect in a lean alloy steel treated by a 'disturbed' bainitic austempering process. *Heat Treat. Surf. Eng.* **2019**, *1*, 72–77. [CrossRef]
64. Emadoddin, E.; Akbarzadeh, A.; Daneshi, G. Effect of intercritical annealing on retained austenite characterization in textured TRIP-assisted steel sheet. *Mater. Charact.* **2006**, *57*, 408–413. [CrossRef]
65. Soleimani, M.; Kalhor, A.; Mirzadeh, H. Transformation-induced plasticity (TRIP) in advanced steels: A review. *Mater. Sci. Eng. A* **2020**, *795*, 140023. [CrossRef]